



ORIGINAL RESEARCH ARTICLE

Study on Corrosion Performance of Friction Stir Processed AA6082-4 wt.% Al₃Zr In Situ Composites

Li Hui , Han Xudong, He Wei, Sun Caizhi, Zhang Xiaolong, Wang Gonglin, Wang Xinyao, Qiao Yuanpeng, Oleksandr Shcheretskyi, and Shcheretskyi Volodymyr

Submitted: 16 October 2023 / Revised: 14 April 2024 / Accepted: 9 May 2024

The 4-mm AA6082-4 wt.% Al₃Zr in situ aluminum matrix composites were processed by friction stir processing. The grain morphology and grain boundary characteristics of the aluminum matrix composites before and after friction stir processing were studied by electron backscatter diffraction and orientation imaging analysis software, and the corrosion behavior of the composites was also studied. The results show that during friction stir processing, the metal undergoes thermoplastic deformation, and the coarse grains of the base metal are refined. The dislocations in the grains are blocked and recombined, and shear texture and deformation substructure are formed simultaneously. With the refinement and dispersion of reinforcement particles (Al₃Zr) after friction stir processing, the ability to reduce the corrosion rate of composites in NaCl solution is improved, the distribution uniformity and stability of passivating film are improved, and the corrosion current density in electrochemical corrosion process is reduced. When the rotating speed is 1200 r/min, the corrosion current density decreases from 5.06×10^{-6} to 1.19×10^{-6} A/cm². The corrosion potential of the stirring zone is about -609 to -580 mV, and the corrosion voltage of the base metal zone is about -52 to -494 mV. After 14 days of immersion testing, the average depth of the corrosion pit is 12.9 μm.

Keywords Aluminum matrix composite, corrosion performance, friction stir processing, in situ

1. Introduction

In recent years, particle-reinforced aluminum matrix composites (AMCs) have attracted much attention (Ref 1-4). Because of its lightweight, high strength, and low manufacturing cost advantages, it can be widely used as structural parts in aerospace and other industries (such as aircraft hydraulic pipe, helicopter landing gear, etc.) (Ref 5-8). In traditional manufacturing, reinforcement particles (ceramic particles) are usually added to the aluminum matrix by stirring casting, and their sizes are mostly microns (Ref 9-11). With the development of modern industry, the requirements for metal composite materials are constantly increasing. Under such a research background, it is necessary to study the adding process of reinforcement particles from a new angle (Ref 12-15). On the one hand, the addition of a nano-scale reinforcing phase helps the aluminum matrix to obtain better performance (Ref 16-19); on the other hand, through the research and design of the in situ process, nano-scale reinforcement particles are grown in situ in

the aluminum matrix, thus obtaining in situ aluminum matrix composites (Ref 20-22).

The reaction of the aluminum matrix with the added initial reactants obtains the reinforcement particles in in situ aluminum matrix composites. The particles obtained by this method have the advantages of smaller size, relatively uniform distribution in the matrix, and better chemical compatibility with the matrix alloy (Ref 23-26). At the same time, compared with the external method, the material obtained by this method shows better mechanical properties. The in situ reaction mechanism and microstructure of composites have been widely studied, and the preparation technology is relatively mature. However, in the preparation process of in situ aluminum matrix composites, some reinforcement particles will inevitably cluster and aggregate, and the internal grains of as-cast materials are coarse, which limits the strength and corrosion resistance of in situ aluminum matrix composites (Ref 27-30).

Friction stir processing (FSP), a new processing technology that originated from friction stir welding (FSW), is widely used in the preparation and surface processing of metal composites (Ref 31-34). As a solid-state processing technology, FSP can refine grains, and land can refine and diffuse the reinforcement particles (Ref 6, 35). In addition, FSP can reduce the deformation of the matrix material, which results in good properties of the composite material (Ref 36-40). Liu et al. (Ref 41) prepared graphene-reinforced AMCs by FSP, and the hardness and conductivity of the composites were improved. Palanivel et al. (Ref 42) successfully synthesized AA6082-(TiB₂ + BN) aluminum matrix composites by friction stir processing. The addition of BN nanoparticles enhanced the wear resistance of AA6082/TiB₂ composites, acting as a solid lubricant and forming a friction film. The addition of TiB₂ and BN as dispersed particles was beneficial to reduce surface wear.

Li Hui, Han Xudong, He Wei, Sun Caizhi, Zhang Xiaolong, Wang Gonglin, Wang Xinyao, and Qiao Yuanpeng, School of Materials Science and Engineering, Jiangsu University of Science and Technology, Zhenjiang 212000, China; Oleksandr Shcheretskyi and Shcheretskyi Volodymyr, Phisico-Technological Institute of Metals and Alloys of the National Academy of Sciences of Ukraine, Kyiv, Ukraine. Contact e-mail: lihuiwind@163.com.

Selvakumar et al. (Ref 43) tried to prepare stainless steel (SS) particle-reinforced aluminum matrix composites by friction stir processing. SS particles were effectively embedded in the aluminum matrix as an alloy without any harmful interface reaction. The addition of SS particles improved the tensile strength of the composites, which ensured the plasticity of the composites at the same time. Researchers have tried to use different reinforcement particles in the field of friction stir processing to prepare aluminum matrix composites with excellent properties, and some researchers have been attempting to study new ways of friction stir processing. Huang et al. (Ref 44) effectively dispersed titanium (Ti) particles into a 5083Al matrix by multi-pass submerged friction stir processing. The multi-pass water cooling process could ensure the rapid acquisition of uniformly diffused particles, the absence of Al/Ti interface reaction produced, and the formation of ultrafine grains. The prepared aluminum matrix composites produced ultrafine grains with an average size of about 1 μm .

Most of the research on AMCs by FSP technology mainly focuses on improving mechanical properties and wear resistance. There have been several international studies on the corrosion properties of metal matrix composites (Ref 45-47). Mirian Mehrian et al. (Ref 48) found that the inhomogeneity of a high fraction of reinforced nanoparticles could increase the corrosion rate in the stirred zone by more than 140 times as compared to primary alloys. This was attributed to secondary phase interfaces and nanoparticle aggregation at grain boundaries, which promoted galvanic coupling corrosion and pitting phenomena. Therefore, it is necessary to study the effect of the distribution of nano-reinforcement particles on the corrosion performance of AMC.

In this study, the in situ AA6082-4wt.%Al₃Zr AMC was reprocessed using the FSP technique with different rotational speeds to change the distribution and the size of Al₃Zr reinforcement particles in the aluminum matrix. The effects of different rotational speeds of FSP on the microstructure and corrosion resistance of AA6082-4wt.%Al₃Zr AMC were investigated by microstructural characterization and corrosion testing of AA6082-4wt.%Al₃Zr AMC after FSP. This study will provide a theoretical and practical basis for the experimental research and industrial application of AMC prepared by FSP in terms of corrosion resistance.

2. Experimental Procedures

2.1 Preparation of the AMCs

The in situ composite was prepared based on AA6082 aluminum alloy in this experiment. The composites were prepared by in situ chemical reaction of the Al-K₂ZrF₆ system. The K₂ZrF₆ powder was placed in a resistance furnace and dried at 473 K for 2 h to remove water. The average particle size of K₂ZrF₆ powder particles was 150 μm . AA6082 aluminum alloy was melted in a graphite crucible and heated to a preparation temperature of 1023 K. As shown in Fig. 1, K₂ZrF₆ powder was put into the melt with an additional ultrasonic field stirring to react fully with the AA6082 melt. The ultrasonic vibration power was 250W, and the duration was 20 minutes. We added C₄Cl₄ refining agent refining and degassing after the reaction. When the melt cooled to 983 K, we skimmed slag to remove by-products such as Na₂O and KF.

Then, the melt was poured into the pre-heated copper model to obtain the in situ Al₃Zr particle-reinforced aluminum matrix composite.

2.2 FSP

In this experiment, in situ Al₃Zr/AA6082 aluminum matrix composites were used, and the content of the reinforced phase Al₃Zr was 4 wt.%. The composites were cut into 90 mm \times 90 mm \times 4 mm flat plates for friction stir processing. FSW-3LM-002 gantry welding machine developed by Beijing Saifoster Technology Company was used for friction stir processing. The stirring head was made of H13 die steel, with a shoulder diameter of 15 mm and a pin length of 3.85 mm. The moving speed of the stirring head was fixed at 100 mm/min, and the rotating rates were 800 r/min, 1000 r/min, and 1200 r/min, respectively. After friction stir processing, the samples required for the electrochemical, immersion, and micro-area electrochemical tests were cut from the cross section perpendicular to the direction of friction stir processing. Figure 2(a), (b) shows the machining schematic and (c) shows the actual sample.

2.3 Electrochemical Test

(1) Polarization Test

Electrochemical test samples were prepared by intercepting the area under a stirring pin. The measuring instrument was a Metrohm electrochemical workstation, and the scanning rate of the polarization curve was 2 mV/s. After the test, the electrochemical parameters, such as corrosion potential E_{corr} , corrosion current density I_{corr} , etc., were obtained by Tafel fitting the data through fitting software (Origin and built-in plugins Tafel Extrapolation).

(2) Electrochemical Impedance Spectroscopy Test

The measuring instrument was the Metrohm electrochemical workstation, which measures the Electrochemical Impedance Spectroscopy (EIS) at corrosion potential. The excitation signal selected an AC sine wave with an amplitude of 5 mV, with a frequency range of 0.1 \sim 1 \times 10⁵ Hz.

The electrochemical test used the three-electrode system, with a friction stir processed aluminum matrix composite sample as the working electrode, platinum sheet as the auxiliary electrode, and saturated calomel electrode (SCE) as the reference electrode. The medium used in the experiment was all 3.5% NaCl solution.

2.4 Immersion Test

The testing area of the immersion test included the stirring zone, thermo-mechanically affected zone, heat-affected zone, and base material. The immersion test simulated the seawater environment, and the corrosion medium was a 3.5% NaCl solution. The immersion test was carried out by in situ corrosion, and marks were made on different areas of the polished joint surface. Then, the morphology near the marks was recorded under SEM. The sample was put into a corrosive medium at constant temperature for continuous corrosion and removed after 7 and 14 days. Subsequently, we put the samples into ethanol for ultrasonic cleaning for 10 min. Finally, the samples were subjected to scanning electron microscopy to observe the corrosion morphology.

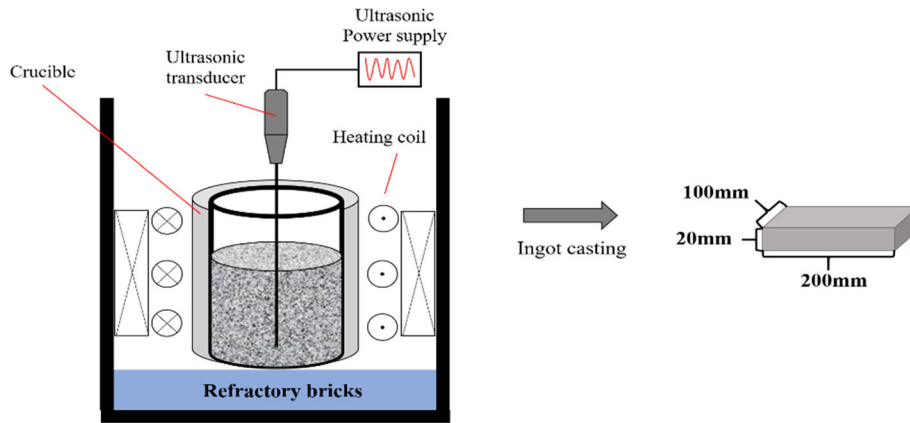


Fig. 1 AA6082-4%wt. Al_3Zr in situ composite preparation process

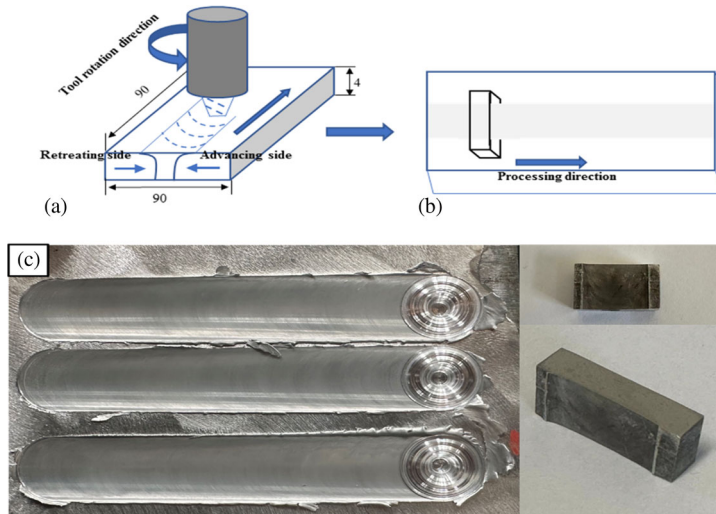


Fig. 2 Schematic diagram of the friction stir processing and characterization test sample

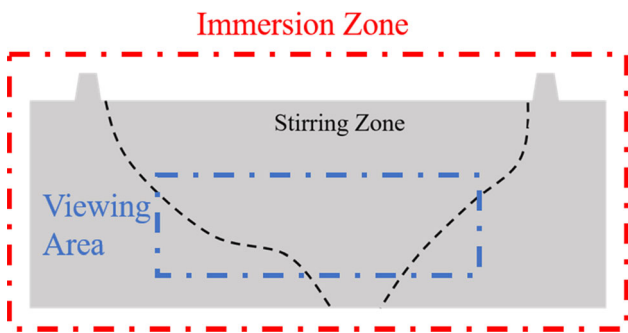


Fig. 3 Schematic diagram of immersion test

2.5 Micro-area Electrochemical test

The interception area of the micro-area electrochemical test was the same as that of the immersion test. The micro-area electrochemical performance of friction stir welded joints with different parameters was tested by using the micro-area electrochemical microscope of Princeton Company. We polished the surface of the friction stir processing sample, scanning the polished surface with a Kelvin probe and moving the scanning area from the center of the stirring area to the base

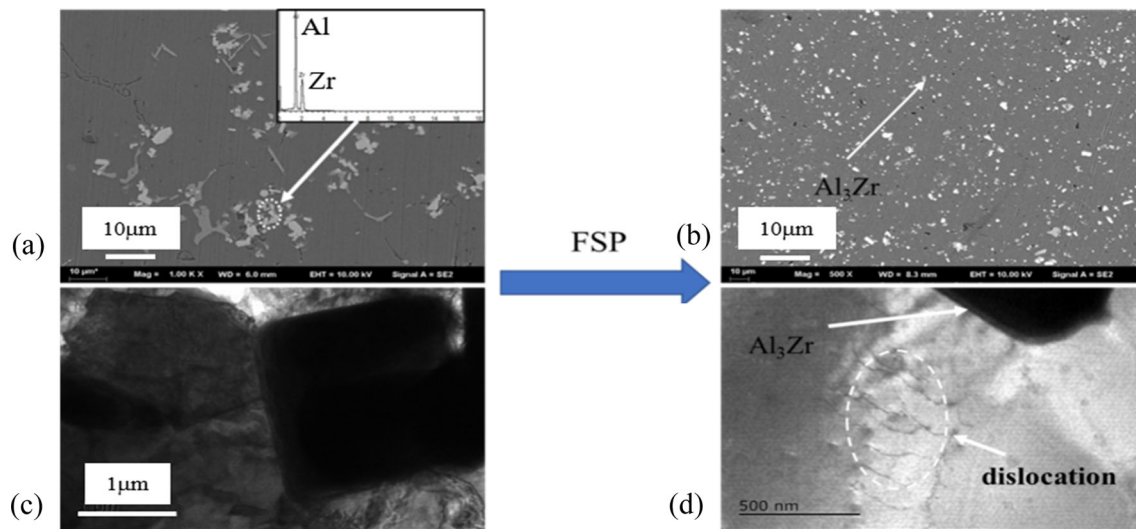
material area. The scanning range of the sample was 5 mm*5 mm, and the scanning step was 40 μm (Fig. 3).

3. Results

3.1 Microstructure of Friction Stir Processed Joints

Figure 4 shows the distribution of reinforcement particles of $Al_3Zr/AA6082$ aluminum matrix composite before and after friction stir processing. The second-phase particles (Al_3Zr) in the composite are generated by in situ self-generation and bonded well with the interface of the aluminum matrix. Due to the limitation of casting conditions, some second-phase particles cluster in the as-cast material, as shown in Fig. 4(a). After friction stir processing, the stirring pin violently stirs the second-phase particles, and the particle shape, size, and distribution state change significantly. Figure 4(b) shows that after friction stir processing, Al_3Zr particles are dispersed and distributed in the matrix, and the particle size is also significantly reduced, which plays a vital role in the homogenization and strengthening of the composite structure.

As shown in Figure 4(e), the average size of the Al_3Zr particles is about 1.56 μm , with more than 75% of the particles



Elemental	Quality(%)	Atomic(%)
Al	68.56	88.09
Zr	31.44	11.91
Total	100	100

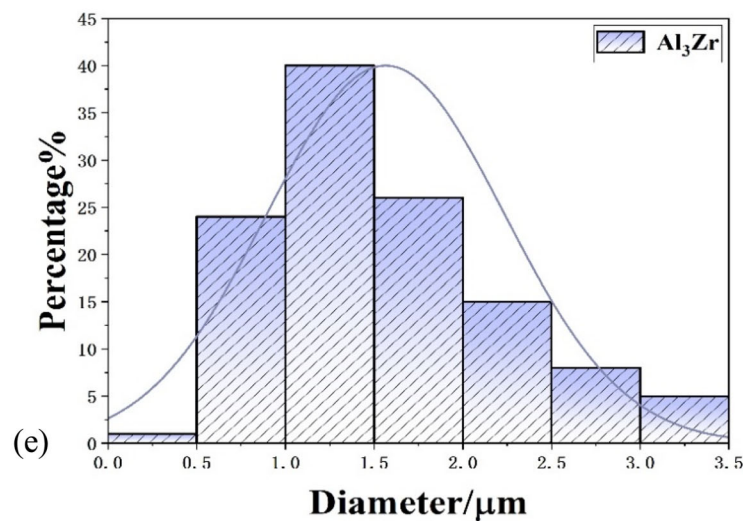


Fig. 4 Microscopic topography of the particles (a), (c) base metal, (b), (d) after FSP; (e) statistical graph of particle size after FSP

having a size of less than $2 \mu\text{m}$. TEM is used to characterize the microstructure of the stirring zone. Figure 4(d) shows that a dislocation layer appears around the fine particle Al_3Zr under the observation of TEM. This is due to the fact that the shear force generated by the stirring pin causes the dislocations in the grain to reorganize and form a dislocation layer. The dislocation layer strengthens the Al_3Zr particles and hinders the dislocation motion.

3.2 Micro-texture of Friction Stir Processed Joints

Figure 5 shows the IPF (Inverse Pole Figure) of the friction stir processing joint of the $\text{Al}_3\text{Zr}/\text{AA6082}$ composite. According to EBSD calculation, the composite in the initial as-cast state has a prominent grain size, irregular shape, and blocky

shape. Figure 5(d) shows that the average grain size in the base metal area is $70\text{-}80 \mu\text{m}$. The grain orientation distribution is random, among which many grains have similar normal orientation along the $\langle 101 \rangle$ direction. The grains with similar average exposure to the $\langle 111 \rangle$ and $\langle 001 \rangle$ directions are less distributed in the base metal. This is because the composite material is cast by liquid metal, and there is no preferential tendency in a particular property. Figure 5(a), (b), and (c) shows IPF diagrams of the Nugget Zone of the composite material after friction stir processing at rotating speeds of 800 r/min , 1000 r/min , and 1200 r/min , respectively. It can be seen from the figure that after friction stir processing, the original grain size of the base metal is significantly reduced, the as-cast structure is severely plastically deformed by the vigorous stirring of the stirring pin, the internal system is

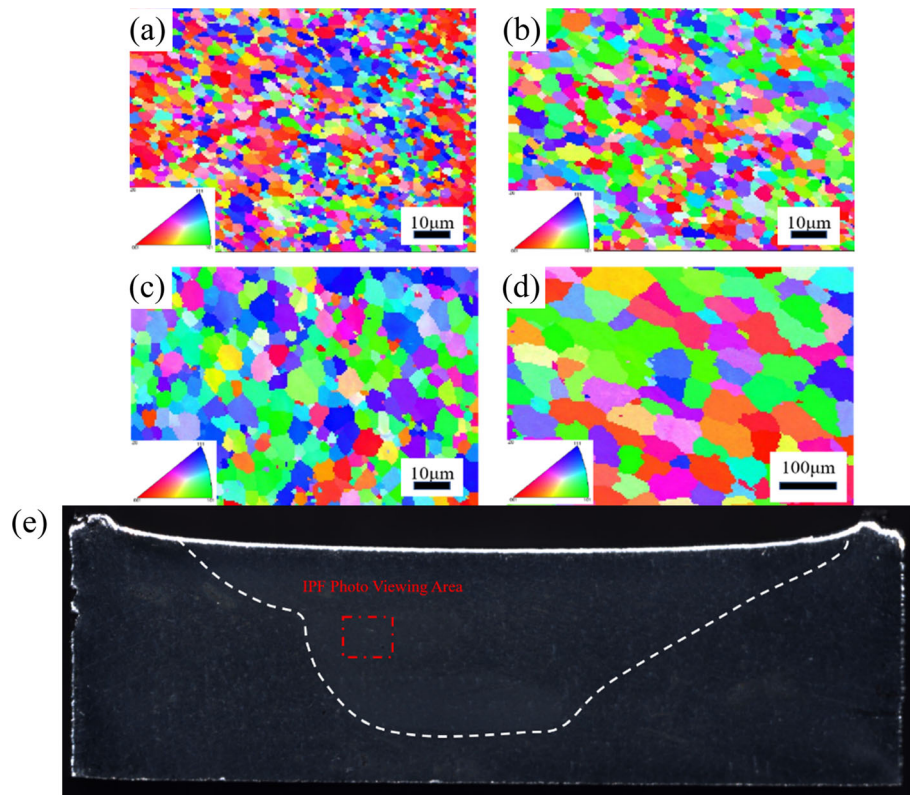


Fig. 5 IPF of FSP joint (a) 800 r/min, (b)1000 r/min, (c)1200 r/min, (d)base metal, (e) IPF photo selection schematic

entirely broken, and the grain undergoes a dynamic recrystallization process at the peak temperature caused by friction of the stirring pin. When the rotating speed is 800 r/min, the grains nucleate and grow under the action of the thermal cycle. Because of the rapid process of heat input, the grain growth is restricted, the grain size is reduced from the original 70-80 μm to 4-5 μm , and the shape is changed from block to fine equiaxed grain. When the rotating speed increases, the effect of considerable heat input on grain growth is weakened, and the grain size slightly increases compared with that at low rotating speed. When the rotating speed is 1200 r/min, the average grain size is 6-7 μm . Figure 5(a), (b), and (c) shows that after friction stir processing, there is a tendency of preferred orientation of grains in the stirring zone because the metal entirely flows during the stirring process. The structure is acted by the shearing force of the stirring pin, and there is some shearing texture. With the increased rotating speed, the distribution number of grains with similar normal orientation to $\langle 001 \rangle$ direction in the stirring zone shows a downward trend. The distribution number of grains with similar normal orientation to $\langle 101 \rangle$ direction shows an upward trend.

Figure 6 shows the characteristic deformation diagram of the friction stir processing joint of the $\text{Al}_3\text{Zr}/\text{AA6082}$ composite. In the figure, the blue part is a recrystallized structure, the yellow part is a substructure structure, and the red part is a morphed structure. The composite is formed by liquid metal casting, cooling, and crystallization, and its microstructure is almost recrystallized, with a small amount of substructure. Because it has not been subjected to secondary deformation processing, it contains a small amount of deformed microstructure inside, and the proportion of three kinds of grains in the base metal area is 88.9%, 9.5%, and 1.5%. After friction stir processing, the

grains in the stirring zone are refined compared with the base metal. The grains in the stirring zone undergo thermoplastic deformation, the dislocations in the grains recombine and accumulate, and the metal dynamically recovers and recrystallizes. Under the shear action of the stirring pin, the distortional strain energy stored in the grain boundary and grain can cause the deformation and reorganization of the metal structure. The figure shows that the proportion of the variable morphology structure in the stirring zone is significantly increased compared with the base metal. Under the rotating speed of 800 r/min, the proportion of the variable morphology structure in the stirring zone is 25.3%. With the increase in rotating speed, the heat input generated by the rotation of the stirring pin continues to increase, and the temperature space for the growth of the crushed grains increases; the proportion of variable morphology tissue showed a downward trend, and the proportion of variable morphology tissue at 1000 r/min and 1200 r/min was 16.4% and 11.7%, respectively. After dynamic recrystallization, the grains in the stirring zone are still mainly recrystallized, accounting for 68.5%, 76.1%, and 60%, respectively. Similarly, with the increase in rotating speed, the dislocation density continues to increase, and the proportion of substructure grains in the stirring zone shows an upward trend, rising from 6 to 29.5%.

Figure 7 shows the distribution of grain orientation difference of $\text{Al}_3\text{Zr}/\text{AA6082}$ composite friction stir processed joint. The grain boundaries shown in the green part of the figure are those with grain orientation differences greater than 2° and less than 15° , that is, low-angle grain boundaries. The grain boundaries shown in the black part are those with grain orientation differences greater than 15° , that is, high-angle grain boundaries. It can be seen from the figure that the

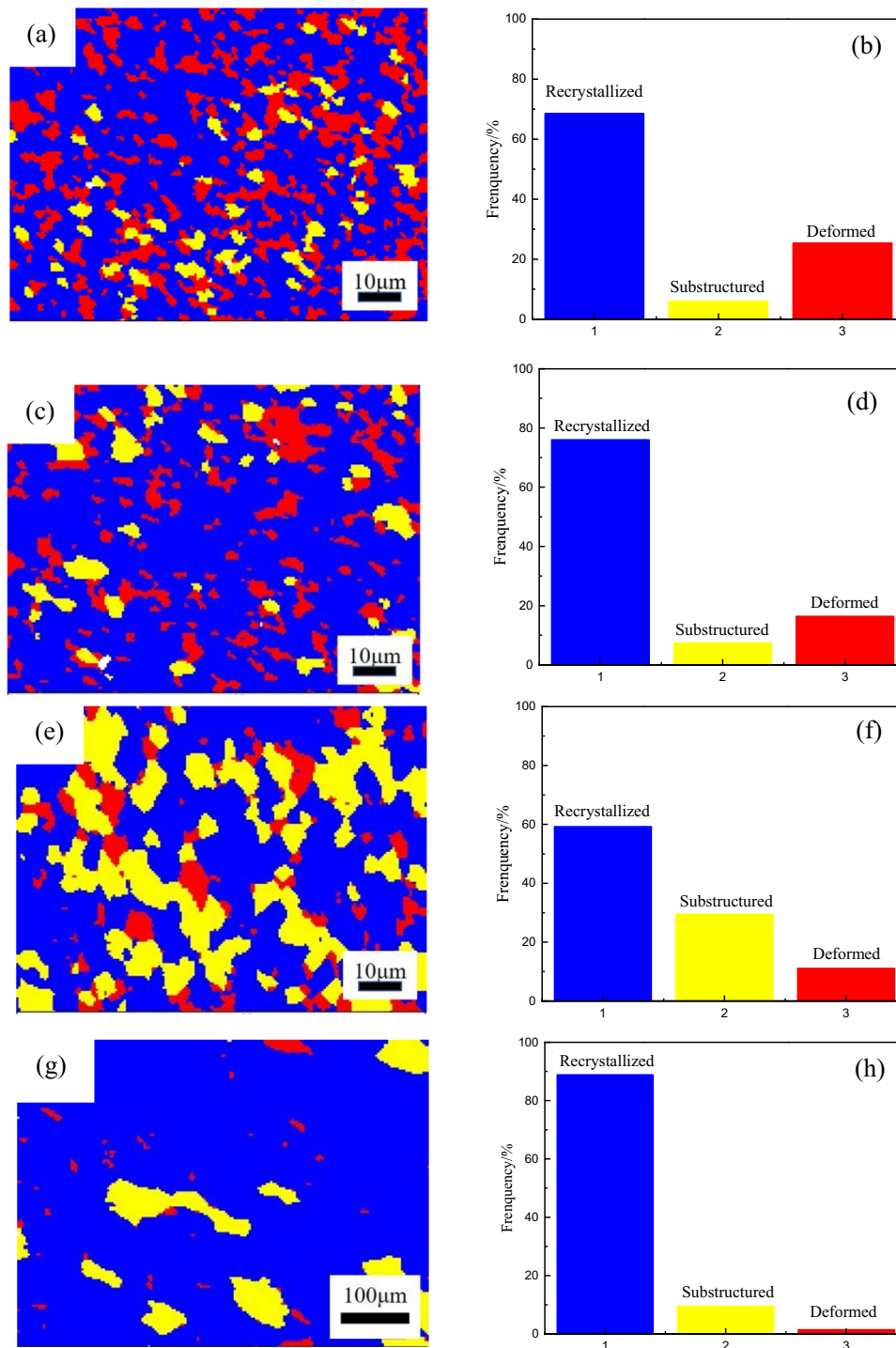


Fig. 6 Deformation characteristics of different regions of FSP joint (a)(b)800 r/min, (c)(d)1000 r/min, (e), (f) 1200 r/min, (g), (h) base metal

orientation difference between grains of the base metal as cast is almost close to the free orientation difference. The proportion of high-angle grain boundaries is large, accounting for 72.7%, and the proportion of low-angle grain boundaries is 27.3%. During processing, the distortional strain energy produced in grain boundaries and grains can reorganize dislocations to form substructure grains composed of low-angle grain boundaries. Under the thermal cycle, these low-angle grain boundaries with small orientation differences are combined into a large grain by rotation. In the rotation process, some low-angle grain bound-

aries become high-angle grain boundaries, and some low-angle grain boundaries remain. Under the operation of a rotating speed of 1200 r/min, the proportion of low-angle grain boundaries increases to 32.8%. The accumulation and recombination of dislocations cause the increase in grain boundary orientation angle, thus forming high-angle grain boundaries and continuous dynamic recrystallization. At the same time, the grains in the stirring zone are refined due to the shear stress generated by the stirring pin; the refined grains tend to be elongated along the direction of the stirring tangent, thus

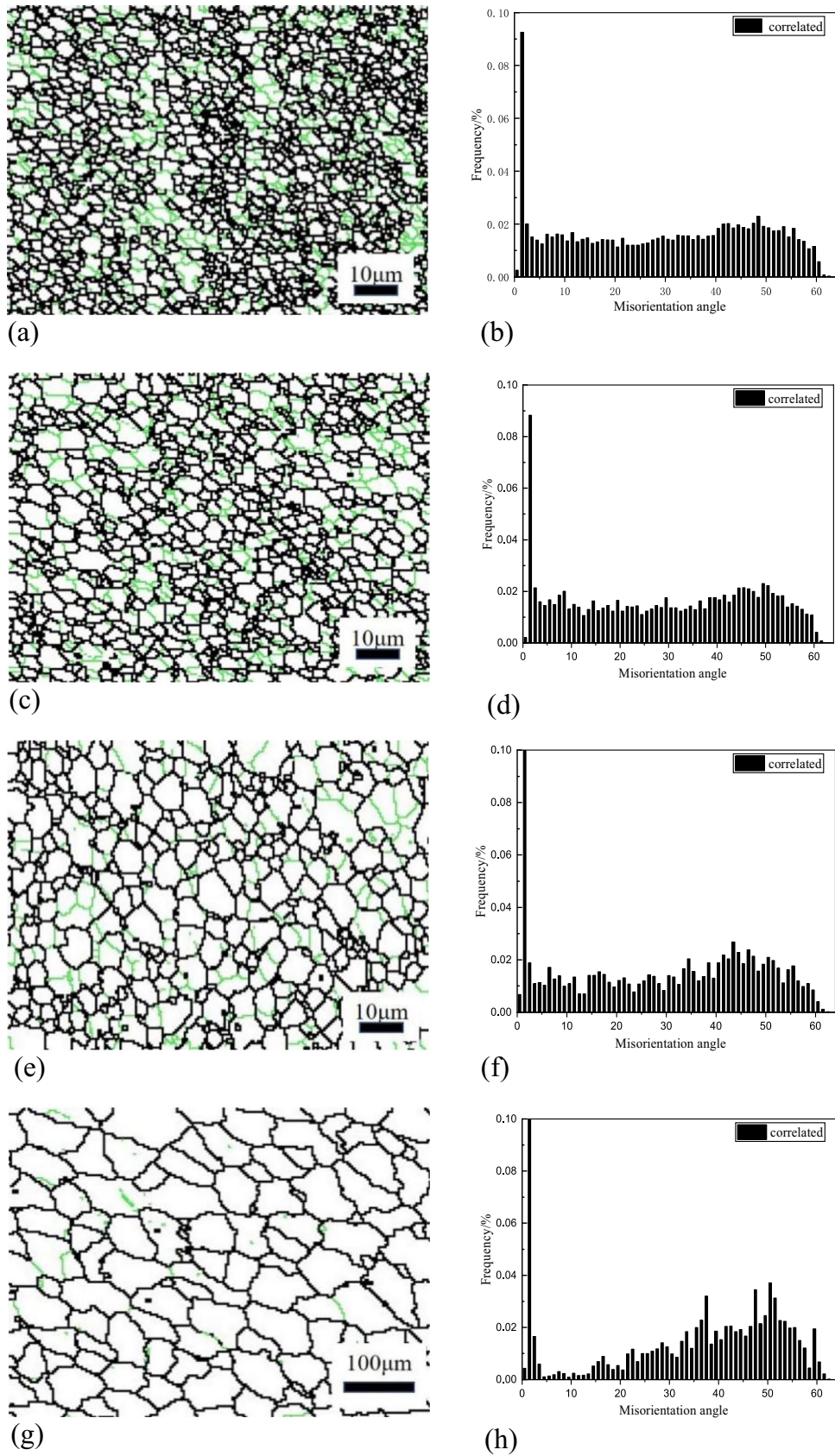


Fig. 7 Distribution of grain orientation difference in different regions of FSP joint. (a), (b)800 r/min, (c), (d)1000 r/min, (e), (f) 1200 r/min, (g), (h) base metal

showing a flat shape. Thermoplastic deformation occurs in the flat and long grains, and the orientation difference between some grains is less than 2° . Some low-angle grain boundaries become high-angle grain boundaries, continuous dynamic recrystallization occurs, and oblate grains deform into equiaxed grains again.

3.3 Immersion Corrosion Morphology of Friction Stir Processed Joints

Figure 8 shows the corrosion morphology of AA6082-4 wt.% Al_3Zr aluminum matrix composites soaked in 3.5% NaCl solution for 7 days and 14 days after friction stir processing with different processes. The Nugget Zone (NZ), Thermo-Mechanically Affected Zone (TMAZ), and Heat-Affected Zone (HAZ) are identified on the map. The demarcation line between the TMAZ and HAZ regions has been blurred due to corrosion from the solution. The second-phase

particle in the composite is the Al_3Zr particle. It can be seen from the figure that local pitting occurs in the stirring zone after friction stir processing, with uniform corrosion morphology and a relatively flat surface. Pitting corrosion also occurs on the base metal's surface; many corrosion products appear and gather, and large corrosion pits are formed on the surface. With the extension of soaking time, it can be seen that the corrosion degree of the base metal zone is further deepened, and corrosion products cover the surface of the base metal zone in a large area. The corrosion degree of the friction stirring processing zone of the three different processes did not significantly deepen with time. The corrosion morphology in the figure shows that the corrosion resistance of in situ $\text{Al}_3\text{Zr}/\text{AA6082}$ aluminum matrix composites has been dramatically improved after friction stir processing.

Figure 9 shows the local in situ corrosion characteristics of $\text{Al}_3\text{Zr}/\text{AA6082}$ aluminum matrix composites and samples

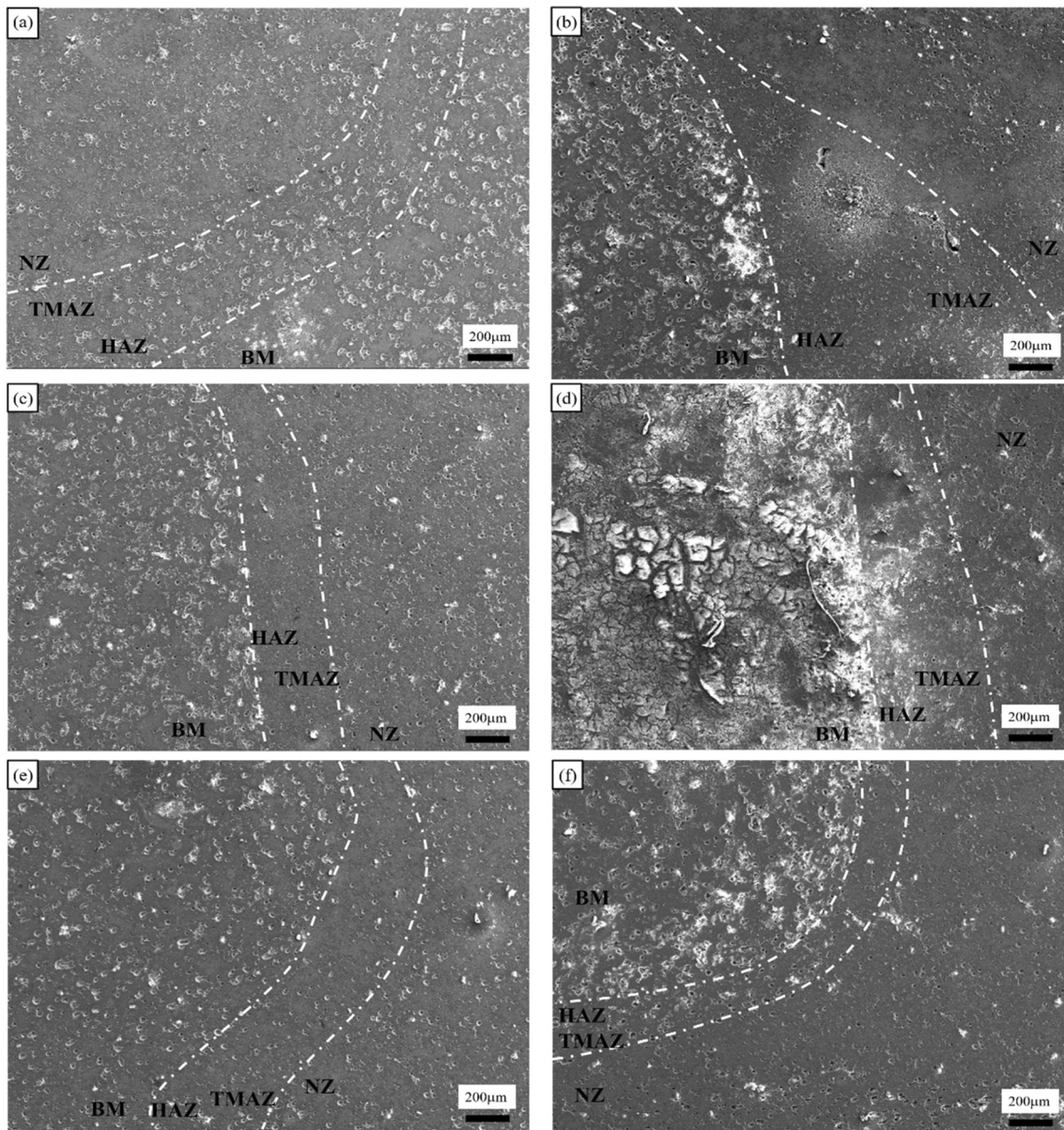


Fig. 8 Corrosion topography of FSP joint. (a), (c),(e) Corrosion morphology after 7 days of 800 r/min, 1000 r/min, 1200 r/min. (b), (d), (f) Corrosion morphology after 14 days of 800 r/min, 1000 r/min, 1200 r/min

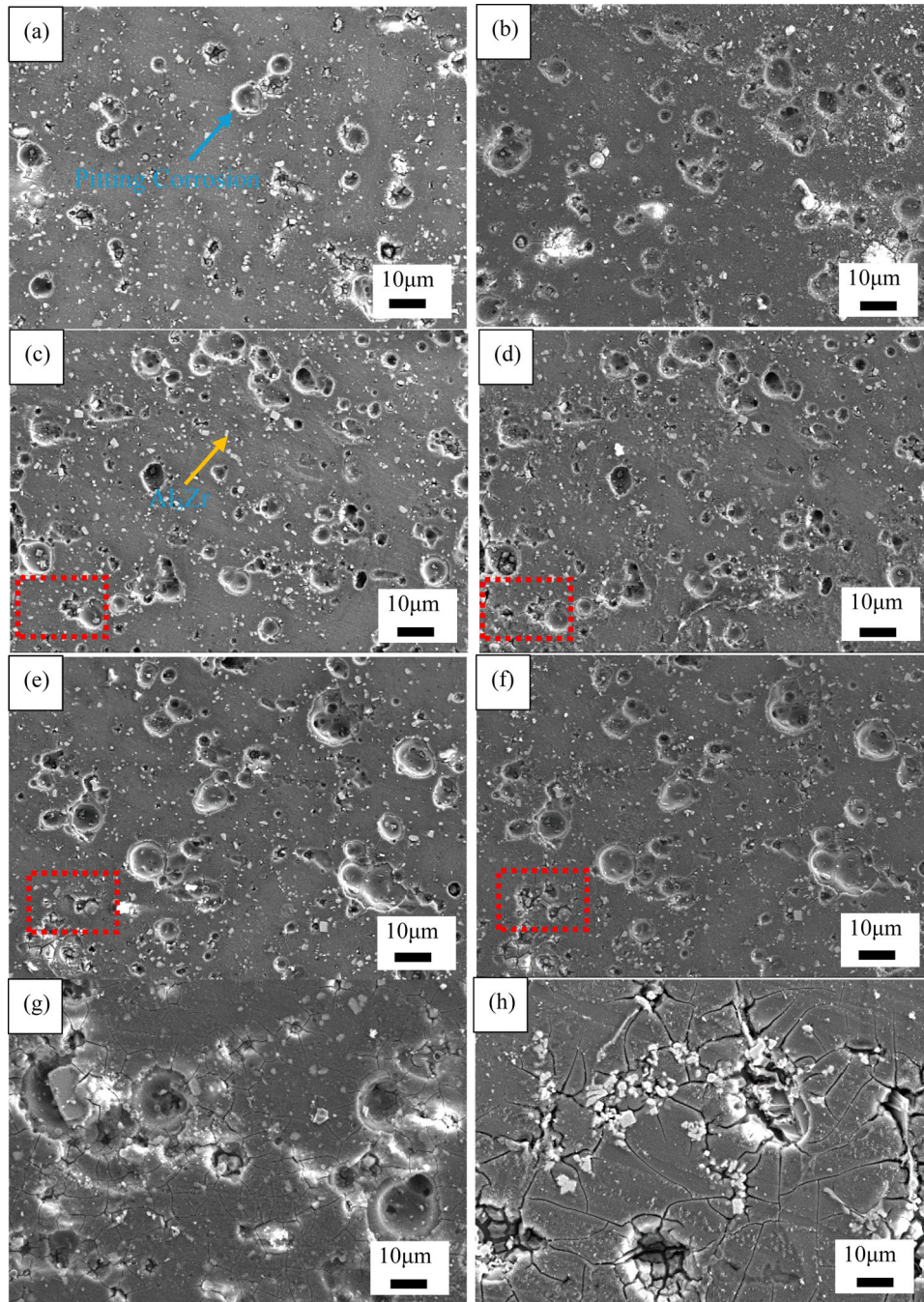


Fig. 9 Corrosion morphology of NZ. (a), (c), (e), (g) Corrosion morphology after 7 days of 800 r/min, 1000 r/min, 1200 r/min, Base Metal. (b), (d), (f), (h) Corrosion morphology after 14 days of 800 r/min, 1000 r/min, 1200 r/min, Base Metal

soaked in 3.5% NaCl solution for 7 days and 14 days after friction stir processing. The figure shows that the reinforcement particles (Al_3Zr) of $Al_3Zr/AA6082$ aluminum matrix composites are uniformly dispersed in the aluminum alloy matrix after friction stir processing, and the particle size is small. By comparing the corrosion pits in the base material (not treated with FSP), we can see that the corrosion pits have deepened and spread to form larger corrosion cracks. The other figures show local pitting corrosion occurred at the edge of the reinforcement particles in the stirring zone and the base metal after soaking in a 3.5% NaCl solution. Due to the Zr element in the reinforced phase, the electrode potential is higher than that of the

aluminum alloy matrix, so the aluminum alloy matrix will preferentially dissolve as an anode, that is, the aluminum matrix in the stirring zone will preferentially dissolve as an anode after 7 days of immersion in the figure, forming small pitting pits. When the rotating speed of friction stir processing is 800 r/min, $Al_3Zr/AA6082$ aluminum matrix composite is sheared by the stirring pin, and severe plastic deformation occurs. The matrix structure is dynamically recrystallized to form uniform and fine equiaxed grains. The recrystallization process is limited by heat input, and grain nucleation and growth are hindered to form smaller equiaxed grains. The degree of tissue homogenization is high, and a relatively small number of pitting pits are formed

after soaking in 3.5% NaCl for 7 days. When the rotating speed of friction stir processing is increased, the heat input generated in the stirring process continues to increase, the inhibition effect on the nucleation and growth of the matrix grains that are stirred and broken is weakened, the grain size gradually increases, and the degree of structural homogenization is enhanced compared with the case of lower rotating speed. However, as the grain size increases, the proportion of grain boundaries per unit area decreases. Due to the higher energy gathered at grain boundaries, this may become a preferred location for corrosion. Therefore, as the percentage of grain boundaries decreases, the overall corrosion resistance of the material is improved. As shown in the figure, when the rotating speed is increased to 1200 r/min, relatively more pitting pits are formed on the surface of the stirring zone after soaking in 3.5% NaCl. Most of the pitting pits appear around the second-phase particles (Al_3Zr). At the same time, a small amount of crack-like corrosion traces also appear on the surface of the stirring zone. These crack-like corrosion traces are intergranular corrosion along the grain boundaries. With the increase in soaking time, the corrosion phenomenon is further deepened. It can be seen from the figure that after 14 days of immersion on the surface of the stirring zone with the rotating speed of 800 r/min, the original size of the corrosion pits has become larger, and more pitting pits have appeared. When the rotating speed is increased to 1000 r/min and 1200 r/min, the deepening of corrosion is inhibited. This is because when the rotating speed is relatively low, the size of the reinforcement particles is relatively large. That is, the area of the cathode particles is relatively large. These larger particles form micro-corrosion coupled with the matrix, producing a large local corrosion current and promoting the accelerated dissolution of the anode. Therefore, larger particles will accelerate the corrosion of the matrix. When the rotating speed of friction stir processing is increased, the size of reinforcement particles (Al_3Zr) gradually decreases, and the distribution is more uniform under the shear action of the stirring pin, which can alleviate the acceleration of the corrosion process. As shown in the figure, when the rotating speed is 1000 r/min and 1200 r/min, the surface corrosion pits have no significant change compared with 7-day immersion after 14 days of sample immersion, the original pitting pits have no apparent expansion, and the number of new pitting pits is also small. As shown in the red dashed portion of the figure, the specimens at 1000r/min and 1200r/min showed new corrosion pits in some areas compared to those at 800r/min and the based material.

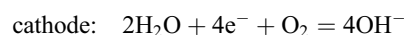
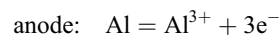
Figure 10 shows the local laser confocal surface morphology of in situ $\text{Al}_3\text{Zr}/\text{AA6082}$ aluminum matrix composites and the samples soaked in 3.5% NaCl solution for 7 and 14 days after friction stir processing. It is evident from the figure that the matrix of the friction stir processed joint appears as pitting pits and the pitting pits expand after soaking. With the increase in soaking time, the transverse area of the pitting pits will increase, and the longitudinal size will deepen. As shown in the figure, the dark dotted parts are pitting pits. When the speed of friction stir processing is 800 r/min, some small-sized corrosion pits are produced after 7 days of immersion, and the average depth of pitting pits is $9.8 \mu\text{m}$. When the rotating speed of friction stir processing increases to 1000 r/min and 1200 r/min, the number of pitting pits slightly increases, and the average depth is $11.3 \mu\text{m}$, $11.6 \mu\text{m}$, respectively. This is because when the rotating speed increases, the heat input generated by stirring increases, the microstructure uniformity obtained is relatively

low, and the tendency to produce corrosion couples is relatively large. With the addition of soaking time to 14 days, the size and depth of corrosion pits on the surface of the stirring zone increased compared with 7 days, and the average depth of corrosion pits increased to $14.6 \mu\text{m}$. The increased rate of corrosion pit depth on the surface of the stirring zone at 1000 r/min and 1200 r/min is slower than that at 800 r/min, and there is no apparent deepening phenomenon. The average depth of the corrosion pit is $13.1 \mu\text{m}$, $12.9 \mu\text{m}$. This is because when the rotating speed is large, the reinforcement particles are increased by the shear action of the stirring pin, the particle size is further reduced, and the distribution is more uniform, the corrosion resistance of the second-phase particles (Al_3Zr) is better, the size is small, and the distribution is uniform, which effectively reduces the corrosion rate of the matrix, thus improving the corrosion resistance of the matrix.

Figure 11 shows the XRD diffraction patterns of the processed samples soaked in 3.5% NaCl solution for 7 and 14 days with different parameters of friction stir processing and the phase analysis of the soaked samples. It can be seen from the figure that the reinforced phase particles of in situ $\text{Al}_3\text{Zr}/\text{AA6082}$ aluminum matrix composites after friction stir processing are still Al_3Zr . The surface of samples with different parameters is oxidized, and oxide Al_2O_3 is produced after soaking. An oxide film is formed on the surface of the sample during immersion to inhibit the corrosion process. The size of Al_3Zr particles in the matrix is significantly reduced, and agglomeration distribution morphology changes after friction stir processing. Al_3Zr particles have high electrode potential and good corrosion resistance. After friction stir processing, the fine and dispersed Al_3Zr particles improve the uniformity of the matrix structure and effectively reduce the corrosion rate. With the extension of soaking time, Al_3Zr -reinforcement particles do not corrode.

3.4 Electrochemical Corrosive Properties of Friction Stir Processing Joints

Figure 12 shows the potentiodynamic polarization curves of in situ $\text{Al}_3\text{Zr}/\text{AA6082}$ aluminum matrix composites and samples after friction stir processing. Tables 1 and 2 shows the corresponding fitting results. The polarization curve comprises a cathode polarization curve and an anode polarization curve. When the aluminum matrix composite is immersed in the corrosive medium (3.5% NaCl solution), the equilibrium electrode potential of the aluminum matrix composite is lower than that of the depolarizer (H) in the medium, and the metal and 3.5% NaCl solution form a corrosion system. At this time, anodic dissolution occurs on the surface of the aluminum matrix composite, and the depolarizer (oxygen molecule) is reduced. The electrochemical reaction formula in the corrosion system composed of aluminum matrix composites and NaCl solution is:



When the corrosion system composed of aluminum matrix composite and NaCl solution is subjected to an electrochemical reaction, the current density of the anodic reaction is expressed in i_a , and the current density of the cathodic reaction is described in i_k . When the corrosion system reaches stability, the aluminum matrix composite is in a self-corrosion state. At this

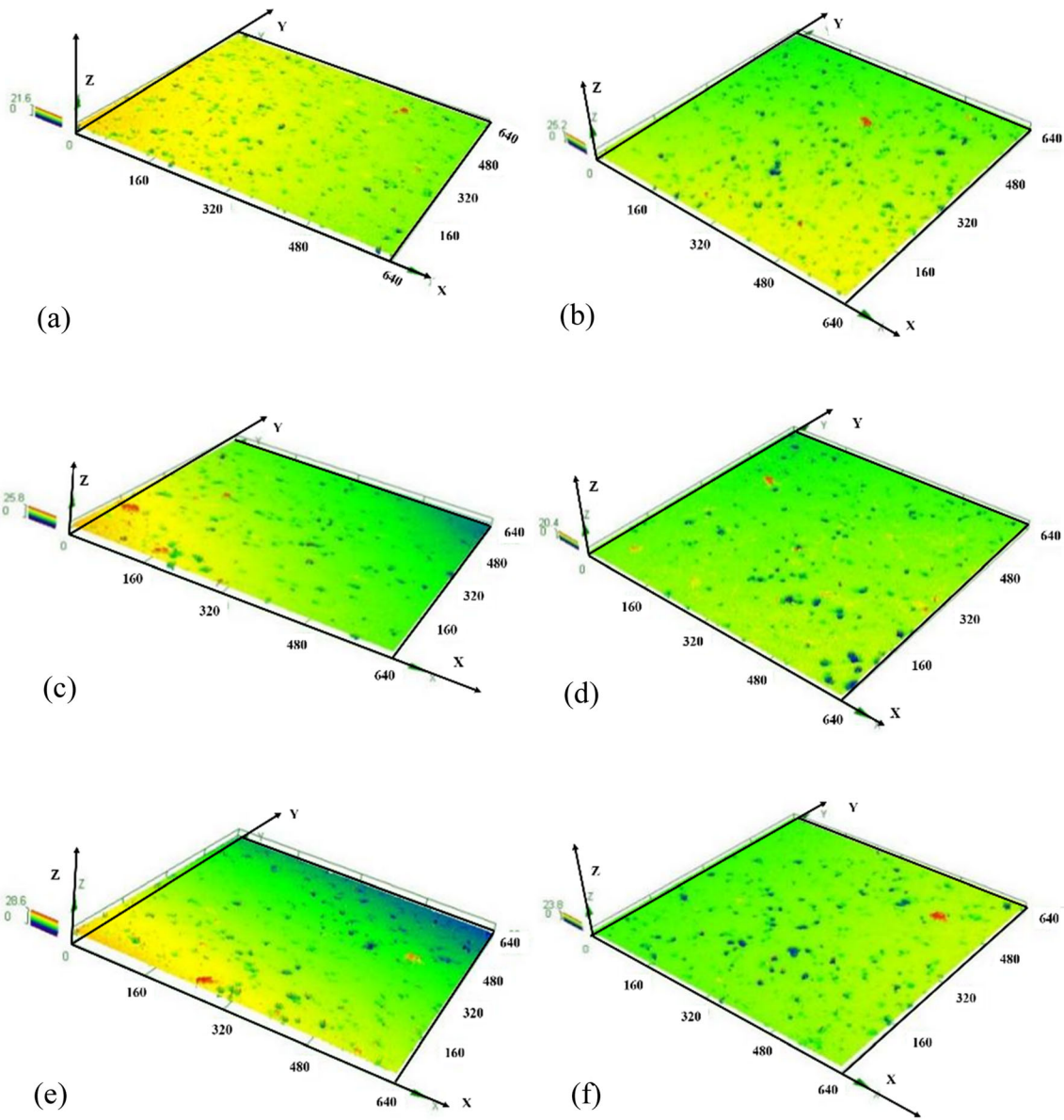


Fig. 10 3D corrosion morphology of FSP joint. (a), (c), (e) Corrosion morphology after 7 days of 800 r/min, 1000 r/min, 1200 r/min. (b), (d), (f) Corrosion morphology after 14 days of 800 r/min, 1000 r/min, 1200 r/min

time, $i_a = i_k = i_{\text{corr}}$ (i_{corr} is corrosion current), there will be no net current accumulation in the corrosion system, and the corrosion system is at a stable potential φ_c . According to Faraday's laws, in the electrolysis process, the amount of reducing substances in the cathode is proportional to the current passing through the corrosion system and the energization time. Therefore, the current density in the anode and cathode represents the corrosion rate in the reaction process of the corrosion system, and the corrosion current density in the self-corrosive state of aluminum matrix composites means its corrosion rate. The externally measured current is zero when the aluminum matrix composite is in the self-corrosive state. Under polarization control, the general equation of metal corrosion rate is:

$$I = i_a - i_k = i_{\text{corr}} \left[\exp\left(\frac{\varphi - \varphi_c}{\beta_a}\right) - \exp\left(\frac{\varphi_c - \varphi}{\beta_k}\right) \right]$$

where I is the external measured current density, i_a is the rate of anodic dissolution of aluminum matrix composites, i_k is the rate of depolarizer reduction, β_a and β_k are, respectively, natural logarithmic Tafel slope of anodic dissolution of aluminum matrix composites and natural logarithmic Tafel slope of depolarizer reduction. When $\varphi - \varphi_c > 0$, anodic polarization occurs in the corrosion system. At this time, the current passing through is anodic current, and the cathodic branch current $i_k = 0$

$$I = i_a = i_{\text{corr}} \exp\left(\frac{\varphi - \varphi_c}{\beta_a}\right)$$

When $\varphi - \varphi_c < 0$, cathodic polarization occurs in the corrosion system. At this time, the current passing through is cathodic current, and the anode branch current $i_a = 0$

$$I = -i_{\text{corr}} \exp\left(\frac{\varphi_c - \varphi}{\beta_a}\right)$$

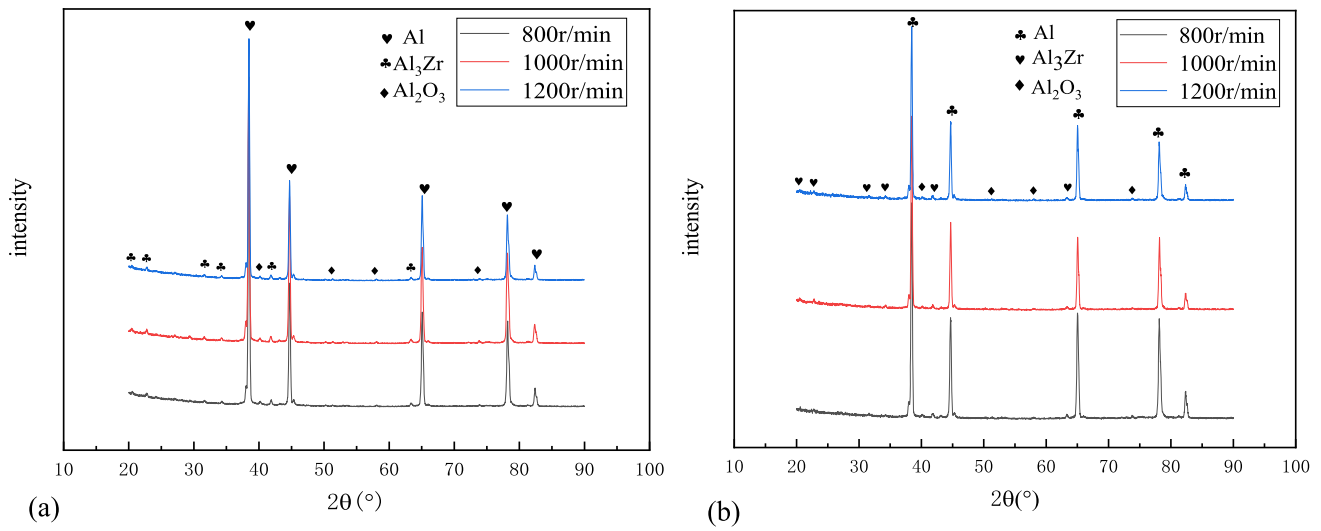


Fig. 11 XRD of FSP joint after corrosion. (a) XRD characterization after 7 days of 800 r/min, 1000 r/min, 1200 r/min. (b) XRD characterization after 14 days of 800 r/min, 1000 r/min, 1200 r/min

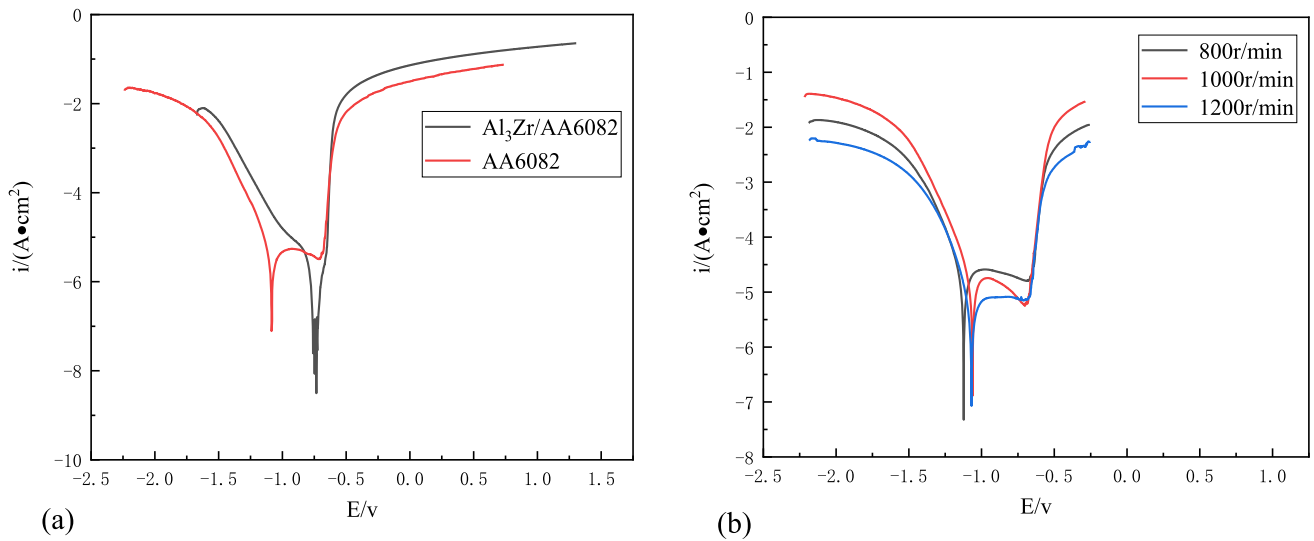


Fig. 12 Polarization curve of base metal and FSP joint. (a) Polarization curve of AA6082 and $\text{Al}_3\text{Zr}/\text{AA6082}$. (b) Polarization curve of FSP joint

Table 1 Fitting results of potentiodynamic polarization curves of AA6082 and $\text{Al}_3\text{Zr}/\text{AA6082}$

Material	E_{corr} mV	i_{corr} mA/cm ²
AA6082	- 1.181	7.6493×10^{-6}
$\text{Al}_3\text{Zr}/\text{AA6082}$	- 0.815	5.0653×10^{-6}

Figure 12(a) shows the polarization curves of 6082 aluminum alloy and $\text{Al}_3\text{Zr}/\text{AA6082}$ aluminum matrix composites. According to the curve trend and fitting results in the figure, with the addition of reinforced phase particles Al_3Zr , the self-corrosion potential E_{corr} of $\text{Al}_3\text{Zr}/\text{AA6082}$ aluminum matrix composites is significantly higher than that of 6082 aluminum alloy, and the corrosion current density i_{corr} is considerably lower. This is because Al_3Zr is metallurgically bonded to the

Table 2 Fitting results of potentiodynamic polarization curves of FSP joint

Rotating speed	E_{corr} mV	i_{corr} mA/cm ²
800 r/min	- 1.123	3.025×10^{-6}
1000 r/min	- 1.060	2.6638×10^{-6}
1200 r/min	- 1.065	1.1998×10^{-6}

matrix by the in situ growth method, and the self-corrosion potential of Al_3Zr particles is high, effectively improving the corrosion resistance of aluminum matrix composites. From the thermodynamic point of view, the formation of the Al_3Zr reinforced phase significantly reduces the corrosion tendency of the matrix material. From the kinetics perspective, in situ Al_3Zr effectively reduces the corrosion rate of aluminum matrix composites. Figure 12(b) shows the polarization curve of the

$\text{Al}_3\text{Zr}/\text{AA6082}$ aluminum matrix composite after friction stir processing with different parameters. According to the fitting results, the self-corrosion potential E_{corr} of $\text{Al}_3\text{Zr}/\text{AA6082}$ aluminum matrix composite after friction stir processing is slightly lower than that of the raw material, which may be due to the size reduction and distribution dispersion of reinforcement particles after friction stir processing, and the formation of countless tiny corrosion couples between fine particles and the matrix. The corrosion tendency of $\text{Al}_3\text{Zr}/\text{AA6082}$ aluminum matrix composites is slightly increased. With the change in rotating speed, the corrosion potential of aluminum matrix composites changes weakly after stirring with different processes. Tables 1 and 2 shows that after friction stir processing, the corrosion current density of $\text{Al}_3\text{Zr}/\text{AA6082}$ aluminum matrix composites is significantly lower than that of raw materials. With the increased rotating speed, the corrosion current density continues to decrease. This is because the distribution and dispersion of Al_3Zr -reinforcement particles with high corrosion potential in the matrix continue to increase after friction stir processing. Countless fine Al_3Zr particles form a passive film in electrochemical corrosion, effectively reducing the electrochemical corrosion rate. In Fig. 12(b), there is a stage in which the current decreases with the increase in potential in the cathodic polarization curve of aluminum matrix composites after three different processes of friction stir processing, which is due to the passivation phenomenon in this stage, resulting in a dense oxide film, which hinders the diffusion of ions in the

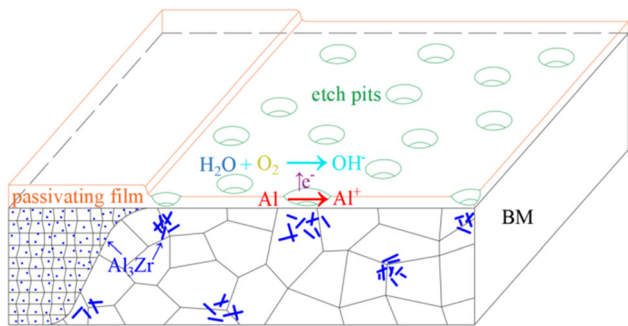


Fig. 13 Corrosion mechanism

polarization process, resulting in the decline of corrosion current. It can also be seen from the figure that the samples at three rotating speeds have an apparent tendency to form passive film during the electrochemical corrosion process. The electrochemical corrosion process and the formation of passive film are shown in Fig. 13. We can find a passive region in the polarization curves of AA6082 and the three FSP samples by comparing the pictures. The resistance to pitting corrosion of $\text{Al}_3\text{Zr}/\text{AA6082}$ is lower than that of AA6082, which may be attributed to the presence of many reinforcement particles agglomerates and pores in the composites, which creates a large number of discontinuities in the surface oxides, enhancing the electrochemical corrosion of the composites' surfaces. In addition, we found that the passive current density of the FSP samples was higher than that of AA6082. According to existing studies, the nature of the grain boundaries gradually shifts from low-angle grain boundaries to high-angle grain boundaries as the material is subjected to FSP. This increases the number of low coordinated lattice points behind the passivation film and, therefore, decreases the integrity and chemical stability of the passivation layer (Ref 49-51). This ultimately leads to the situation in our polarization curves, where the passivating film of the FSP sample has a slightly lower corrosion resistance than AA6082.

Figure 14 shows the AC impedance spectrum of the in situ $\text{Al}_3\text{Zr}/\text{AA6082}$ aluminum matrix composite and the samples after friction stir processing. The AC impedance of the aluminum matrix composite electrode is a complex number, consisting of the real part Z' and the imaginary part Z'' , $Z = Z' + jZ''$. The capacitance loop in the Nyquist diagram represents the corrosion reaction of aluminum matrix composites. In Fig. 14(a), it is reflected that the generation of reinforcement particles (Al_3Zr) reduces the radius of the capacitance loop of aluminum alloy in corrosion solution to a certain extent. The formation of a capacitance loop is related to the passivation layer on the surface of aluminum matrix composites. $\text{Al}_3\text{Zr}/\text{AA6082}$ composite is completed by casting. There is a partially uneven distribution of particles (Al_3Zr) in the material, and the passivation layer formed on the surface of the material is unstable. Charge transfer plays a significant role in the corrosion process. When charge transfer occurs in the corrosion system, the barrier effect of the passivation layer on

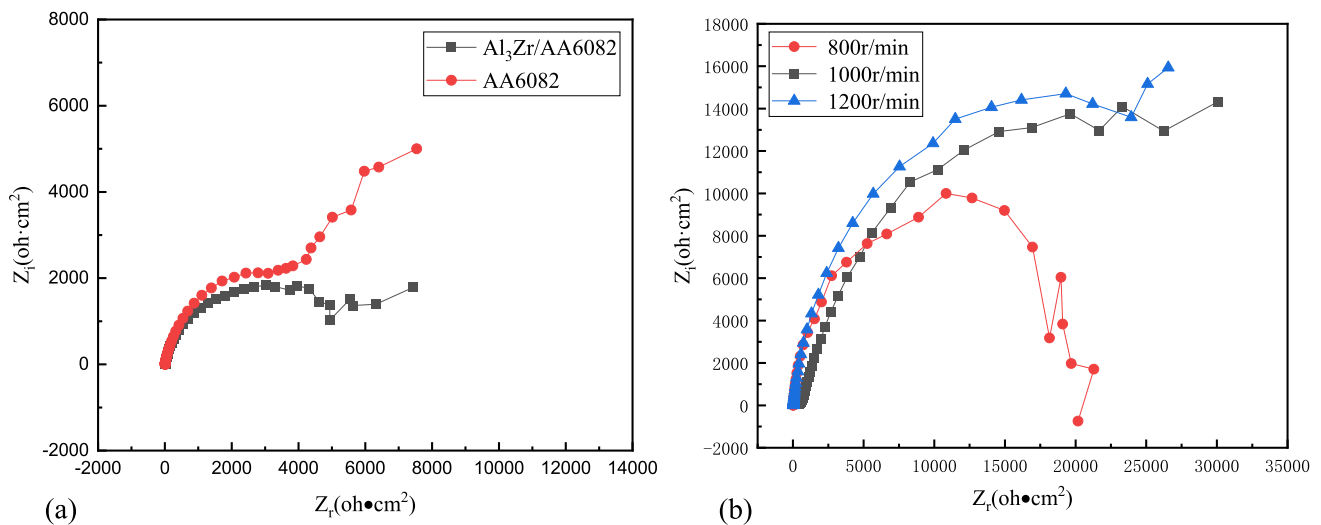


Fig. 14 EIS measurements of the base metal and FSP joint. (a) Nyquist plots of AA6082 and $\text{Al}_3\text{Zr}/\text{AA6082}$. (b) Nyquist plots of FSP joint

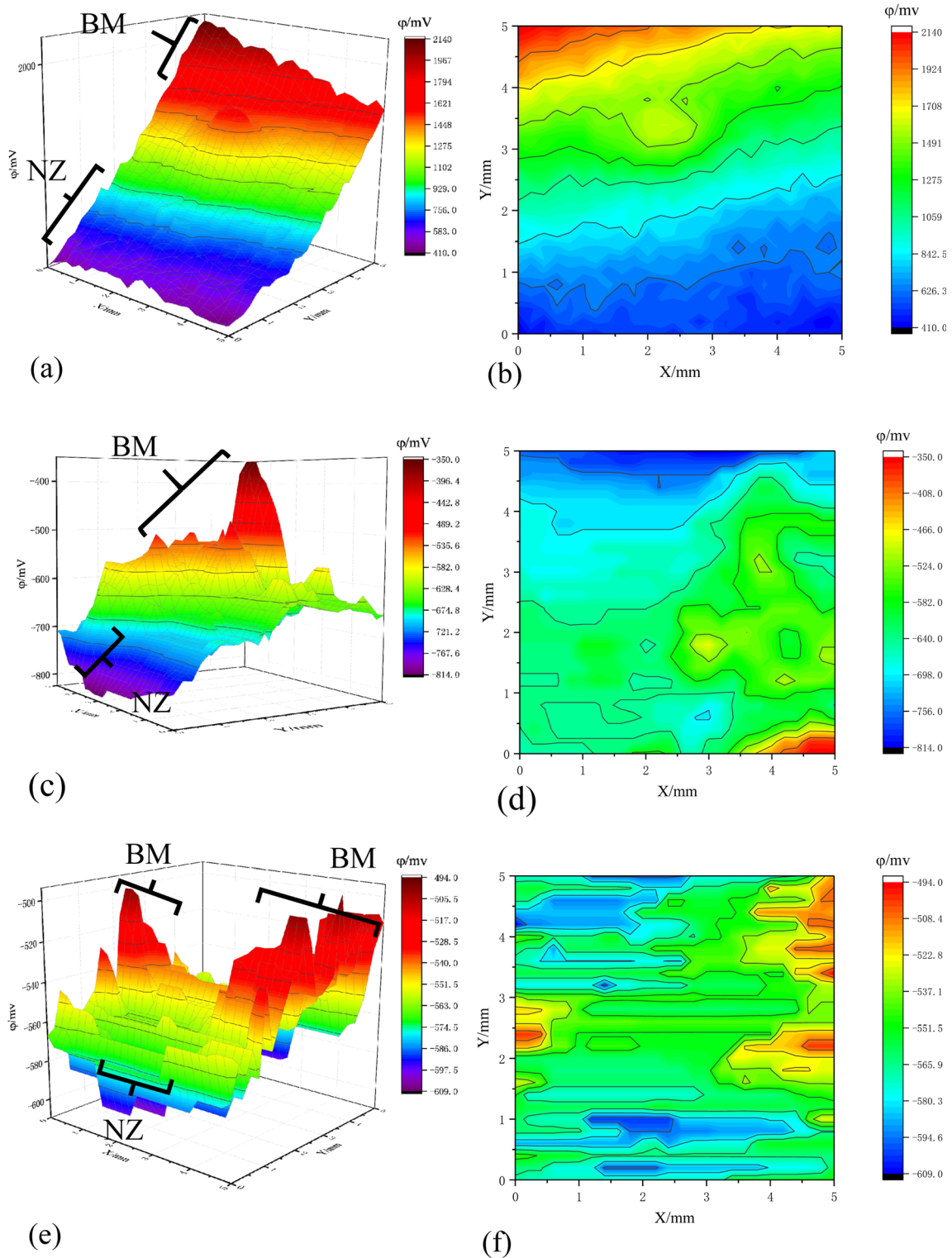


Fig. 15 SKP diagram and contour of FSP joint. (a), (b) 800 r/min, (c), (d) 1000 r/min, (e), (f) 1200 r/min

the composite surface on charge transfer is weakened to a lesser extent. This is also related to the fact that the composites have no obvious passivation stage in the polarization process. After friction stir processing, the microstructure uniformity of the composite and the distribution uniformity of reinforcement particles (Al_3Zr) are significantly improved, and the uniformity of the passivation layer on the surface of the material is

improved. As shown in Fig. 14(b), the materials processed by the three processes form a capacitance loop with a large radius in the corrosion system, which further shows that the microstructure and particle uniformity of the composite material play a vital role in the uniform distribution and stability of the passivation layer.

Figure 15 shows the scanning Kelvin spectrum of samples processed with different parameters of friction stir processing. We have labeled the NZ and BM zones with black lines in Fig. 15(a), (c) and (e). It can be seen from the figure that after friction stir processing, the corrosion potential of the stirring zone is significantly lower than that of the base metal, indicating that the corrosion tendency of the stirring zone is higher than that of the base metal. After friction stir processing, the dispersed reinforced phase particle Al_3Zr makes it easier to form countless corrosion micro couples with the metal matrix, improving the corrosion tendency of the stirring zone. Because the grain size in the base metal area is much larger than in the stirring zone, the distribution of reinforced phase particles also has segregation, and its corrosion tendency is low. When the rotating speed is 800 r/min, the corrosion potential in the stirring zone is about 410 to 842.5 mV, and the corrosion potential in the base metal zone is about 1708 to 2140 mV. When the rotating speed is 1000 r/min, the corrosion potential in the stirring zone is about - 814 to - 698 mV, and the corrosion potential in the base metal zone is about - 466 to - 350 mV. When the rotating speed is 1200 r/min, the corrosion potential in the stirring zone is about - 609 to - 580 mV, and the corrosion potential in the base metal zone is about - 522 to - 494 mV. The results show that when the rotating speed of friction stir processing is 1200 r/min, the corrosion potential difference between the stirring zone and the base metal zone is smaller than the other two rotating speeds. This is because in the friction stir processing process, when the rotating speed of the stirring pin is high, the heat input increases, the structure is subjected to severe plastic deformation, and the degree of recrystallization is high. The size of Al_3Zr -reinforcement particles is significantly reduced, the degree of distribution and dispersion in the matrix is improved, and the uniformity of the matrix structure is improved as a whole. Therefore, the difference between the corrosion potential in the stirring zone and the base metal is small, reducing the corrosion tendency.

4. Conclusion

1. During the friction stir processing of aluminum matrix composites, the coarse grains of the base metal are thermoplastic and deformed due to the shear stress produced by the stirring pin and the shaft shoulder. Under the action of the stirring thermal cycle, the deformed grains are dynamically recrystallized.
2. The corrosion of aluminum matrix composites starts from local pitting, which originates from the second-phase particles (Al_3Zr) and the aluminum matrix at its edge, and the second-phase particles act as the cathode. After 14 days of in situ corrosion, the degree of intergranular corrosion in the friction stir processing zone is relatively light, and severe pitting occurs in the base metal zone. The uniformly distributed second-phase particles and fine equiaxed crystals are the main reasons for the pitting sensitivity reduction in the friction stir processing zone.
3. In the friction stir processing zone of aluminum matrix composites, compared with the base metal, the corrosion current density is reduced, the corrosion rate is significantly reduced, and the capacitive reactance radius is increased. The uniformly distributed second-phase particles

(Al_3Zr) and fine equiaxed grains form a uniform and stable passivation layer on the surface of aluminum matrix composites in the corrosion environment, which effectively hinders the diffusion of ions in the corrosion process.

4. When the rotating speed is 1200 r/min, the corrosion current density is 1.19×10^{-6} A/cm². The corrosion potential of the stirring zone is about - 609 to - 580 mV, and the corrosion voltage of the base metal zone is about - 52 to - 494 mV. Currently, the average depth of the corrosion pit is 12.9 μm . In summary, when the rotating speed is 1200 r/min, the corrosion resistance of the stirring zone is optimal.

Funding

This research was financially supported by the National Natural Science Foundation of China, No. 51605206. Graduate Research and Innovation Projects of Jiangsu Province, No. SJCX23_2181. Ministry of Science and Technology High-end Foreign Experts Introduction Program Project, G2022014043. Ministry of Science and Technology High-end Foreign Experts Introduction Program Project, G2022014134L.

Conflict of interest

The authors declare that they have no conflict of interest.

References

1. H. Kumar, R. Prasad, and P. Kumar, Mechanical and Tribological Characterization of Industrial Wastes Reinforced Aluminum Alloy Composites Fabricated via Friction Stir Processing, *J. Alloys Compd.*, 2020, **831**, p 154832.
2. T. Wang, X. Zuo, and Y. Zhou, High Strength and High Ductility Nano-Ni- $\text{Al}_2\text{O}_3/\text{A356}$ Composites Fabricated with Nickel-Plating and Equal Channel Angle Semi-Solid Extrusion (ECASE), *J. Mater. Res. Technol.*, 2021, **13**, p 1615–1627.
3. D.S. Rao, B.G. Gupta, and T.V. Rao, Mechanical and Microstructural Behaviour of Aluminium/TiB₂ Composites Fabricated Through Multi-pass Friction Stir Processing, *Mater. Today Proc.*, 2021, **44**, p 413–418.
4. L. Jiao, Z.W. Wang, and Y.T. Zhao, Influence of Electromagnetic Ultrasound Dual Field Coupling In Situ Synthesis of ($\text{ZrB}_2 + \text{Al}_3\text{Zr}$)/AA6016 Composites on the Structure and Properties, *Int. J. Metalcast.*, 2023, **17**(3), p 1736–1753.
5. S. Zhang, G. Chen, and J. Wei, Effects of Energy Input During Friction Stir Processing on Microstructures and Mechanical Properties of Aluminum/Carbon Nanotubes Nanocomposites, *J. Alloys Compd.*, 2019, **798**, p 523–530.
6. H. Zhang, B. Zhang, and Q. Gao, A Review on Microstructures and Properties of Graphene-Reinforced Aluminum Matrix Composites Fabricated by Friction Stir Processing, *J. Manuf. Process.*, 2021, **68**, p 126–135.
7. H. Das, M. Mondal, and S.T. Hong, Texture and Precipitation Behavior of Friction Stir Welded Inconel 825 Alloy, *Mater. Today Commun.*, 2020, **25**, 101295
8. V. Murthy, S.D. Kumar, and K.K. Saju, Optimization of Friction Stir Processing Parameters for Manufacturing Silicon Carbide Reinforced Aluminum 7075-T651 Surface Composite, *Mater. Today Proc.*, 2019, **18**, p 4549–4555.
9. J. Zhu, W. Jiang, and G. Li, Microstructure and mechanical properties of $\text{SiC}_{\text{np}}/\text{Al6082}$ aluminum matrix composites prepared by squeeze casting combined with stir casting, *Mater. Process. Technol.*, 2020, **283**, p 116699.

10. M. Agarwal and R. Srivastava, Influence of Fine Al₂O₃ and Aluminium Nano Particles on the 6061 Aluminium Alloy near the Grain Boundary of the Semi-Solid Cast Microstructure, *Trans. Indian Ceram. Soc.*, 2019, **78**(2), p 1–7.
11. S. Behnamfard, R.T. Mousavian, and R.A. Khosroshahi, Semi-Solid Stirring of Modified Ceramic Nanoparticles Using Iron and Nickel in an Aluminum A356 Melt, *Mater. Res. Express.*, 2019, **6**(9), 096553
12. J. Zhang, Q. Liu, and S. Yang, Microstructural Evolution of Hybrid Aluminum Matrix Composites Reinforced with SiC Nanoparticles and Graphene/Graphite Prepared by Powder Metallurgy, *Prog. Nat. Sci-Mater.*, 2020, **30**(2), p 192–199.
13. E. Salur, A. Aslan, and M. Kuntoğlu, Effect of Ball Milling Time on the Structural Characteristics and Mechanical Properties of Nano-Sized Y₂O₃ Particle Reinforced Aluminum Matrix Composites Produced by Powder Metallurgy Route, *Adv. Powder Technol.*, 2021, **32**(10), p 3826–3844.
14. J. Liu, Z. Zheng, and J. Wang, Pressureless Infiltration of Liquid Aluminum Alloy into SiC Preforms to Form Near-Net-Shape SiC/Al Composites, *J. Alloys Compd.*, 2008, **465**(1–2), p 239–243.
15. L. Jiao, B.W. Wang, and Y.T. Zhao, Microstructure and Mechanical Properties of In Situ AlB₂/A356 Composites Under T6 Treatment, *Inter. Metalcast.*, 2023, **17**, p 1082–1094.
16. C.S. Ramesh, A. Ahamed, and B.H. Channabasappa, Development of Al 6063–TiB₂ In Situ Composites, *Mater. Design.*, 2010, **31**(4), p 2230–2236.
17. H. Li, P.Y. Xu, and Y.P. Qiao, Microstructure and Mechanical Properties of Ultrahigh Speed Friction-Stir-Welded Joints of In Situ Al₃Zr Particle Reinforced Aluminum Matrix Composite Sheets, *Adv. Eng. Mater.*, 2021, **23**(8), p 2100295.
18. L. Jiao, F. Li, and Y.T. Zhao, Microstructure and Tribological Behavior of in situ ZrB₂/A356 Composites Prepared Under Magnetic Field, *Surf. Topogr. Metrol. Prop.*, 2021, **9**(1), p 015026.
19. H. Li, P.Y. Xu, and L. Jiao, Surface Wear Behavior and Strengthening Mechanism of Al₃Zr Particle Reinforced Aluminum Matrix Composites Prepared In Situ, *Surf. Topogr. Metrol. Prop.*, 2019, **7**(4), 045013
20. S. Kumar, V.S. Sarma, and B.S. Murty, A Statistical Analysis on Erosion Wear Behaviour of A356 Alloy Reinforced with In Situ Formed TiB₂ Particles, *Mater. Sci. Eng. A*, 2008, **476**(1–2), p 333–340.
21. L. Jiao, F. Li, and Y.T. Zhao, Surface Friction and Wear Behavior of In Situ AlB₂ Particle-Reinforced A356 Composites, *J. Mater. Eng. Perform.*, 2022, **31**, p 5812–5822.
22. H. Li, Y.P. Qiao, and S.B. Lu, Study on Microstructure Evolution and Strengthening and Toughening of Friction Stir Processed AA6082-4%Al₃Zr In-Situ Composites, *J. Mater. Eng. Perform.*, 2022, **31**, p 5221–5230.
23. J. Su, Y. Li, and M.G. Duan, Investigation on Particle Strengthening Effect in In-Situ TiB₂/2024 Composite by Nanoindentation Test, *Mater. Sci. Eng. A*, 2018, **727**, p 29–37.
24. S. Dinesh-Kumar, M. Ravichandran, A. Jeevika, and B. Stalin, Effect of ZrB₂ on Microstructural, Mechanical and Corrosion Behaviour of Aluminium (AA7178) Alloy Matrix Composite Prepared by the Stir Casting Route, *Ceram. Int.*, 2021, **47**, p 12951–12962.
25. K. Liu, Y. Li, and M. Duan, Fatigue Life Prediction of In-Situ TiB₂/2024 Aluminum Matrix Composite, *Int. J. Fatigue*, 2021, **145**, 106128
26. C.Z. Sun, H. Li, and F. Wang, Study on the Microstructure and Mechanical Properties of ZrB₂/AA6111 Particle-Reinforced Aluminum Matrix Composites by Friction Stir Processing and Heat Treatment, *Interface Metalcast.*, 2023, **189**(1), p 457–469.
27. L. Jiao, Z.W. Wang, and Y.T. Zhao, Study on Friction Properties of In Situ Synthesized (AlB₂ + Al₂O₃)/A356 Composite, *J. Mater. Eng. Perform.*, 2023 <https://doi.org/10.1007/s11665-023-08387-2>
28. N. Muralidharan, K. Chockalingam, I. Dinaharan, and K. Kalaiselvan, Microstructure and Mechanical Behavior of AA2024 Aluminum Matrix Composites Reinforced with In Situ Synthesized ZrB₂ Particles, *J. Alloys Compd.*, 2018, **735**, p 2167–2174.
29. Y.T. Zhao, S.L. Zhang, and G. Chen, Aluminum Matrix Composites Reinforced by In Situ Al₂O₃ and Al₃Zr Particles Fabricated via Magnetochemistry Reaction, *Trans. Nonferr. Metal. Soc.*, 2010, **20**(11), p 2129–2133.
30. H.M. Wang, G.R. Li, Y.T. Zhao, and G. Chen, In Situ Fabrication and Microstructure of Al₂O₃ Particles Reinforced Aluminum Matrix Composites, *Mater. Sci. Eng. A*, 2010, **527**(12), p 2881–2885.
31. Y.C. Feng, L. Geng, A.B. Li, and Z.Z. Zheng, Fabrication and Characteristics of In Situ Al12W Particles Reinforced Aluminum Matrix Composites by Reaction Sintering, *Mater. Des.*, 2010, **31**(2), p 965–967.
32. N. Netto, L. Zhao, and J. Soete, Manufacturing High Strength Aluminum Matrix Composites by Friction Stir Processing: An Innovative Approach, *J. Mater. Process. Technol.*, 2020, **283**, 116722
33. L. Jiao, Q.J. Zhang, and Y.T. Zhao, High-Temperature Friction Wear Behavior of (AlB₂ + Al₂O₃)/A356 Composites Regulated by Acoustic-Magnetic Coupling Field, *Int. J. Metalcast.*, 2023 <https://doi.org/10.1007/s40962-023-01130-6>
34. A. Heidarzadeh, S. Mironov, and R. Kaibyshev, Friction Stir Welding/Processing of Metals and Alloys: A Comprehensive Review on Microstructural Evolution, *Prog. Mater. Sci.*, 2021, **117**, 100752
35. M. Orłowska, F. Pixner, and A. Hütter, Manufacturing of Coarse and Ultrafine-Grained Aluminum Matrix Composites Reinforced with Al₂O₃ Nanoparticles via Friction Stir Processing, *J. Manuf. Process.*, 2022, **80**, p 359–373.
36. S. Mabuwa, V. Msomi, N.N. Tsolekile, and V.M. Zungu, Status and Progress on Fabricating Automotive-Based Aluminium Metal Matrix Composites Using FSP Technique, *Mater. Today Proc.*, 2022, **56**, p 1648–1652.
37. K. Zass, S. Mabuwa, and V. Msomi, A Review on Reinforced Particles Used on the Production of FSP Composites, *Mater. Today Proc.*, 2022, **56**, p 2392–2397.
38. V.K. Parikh, A.D. Badgajar, and N.D. Ghetya, Effect of Friction Stir Processing Parameters on Microstructure and Microhardness of Aluminium Based Metal Matrix Composites, *Mater. Today Proc.*, 2022, **62**, p 7455–7460.
39. M. Deepan, C. Pandey, and N. Saini, Estimation of Strength and Wear Properties of Mg/SiC Nanocomposite Fabricated Through FSP Route, *Sci. Eng.*, 2017, **39**, p 4613–4622.
40. N. Saini, C. Pandey, and S. Thapliyal, Mechanical Properties and Wear Behavior of Zn and MoS₂ Reinforced Surface Composite Al–Si Alloys Using Friction Stir Processing, *SILICON*, 2018, **10**, p 1979–1990.
41. Y.J. Liu, G.Q. Chen, and H. Zhang, In Situ Exfoliation of Graphite for Fabrication of Graphene/Aluminum Composites by Friction Stir Processing, *Mater. Lett.*, 2021, **301**, 130280
42. R. Palanivel, I. Dinaharan, R.F. Laubscher, and J. PauloDavim, Influence of Boron Nitride Nanoparticles on Microstructure and Wear Behavior of AA6082/TiB₂ Hybrid Aluminum Composites Synthesized by Friction Stir Processing, *Mater. Design.*, 2016, **106**, p 195–204.
43. S. Selvakumar, I. Dinaharan, R. Palanivel, and B. GaneshBabu, Development of Stainless Steel Particulate Reinforced AA6082 Aluminum Matrix Composites with Enhanced Ductility Using Friction Stir Processing, *Mater. Sci. Eng. A*, 2017, **685**, p 317–326.
44. G.Q. Huang and Y.F. Shen, The Effects of Processing Environments on the Microstructure and Mechanical Properties of the Ti/5083Al Composites Produced by Friction Stir Processing, *J. Manuf. Process.*, 2017, **30**, p 361–373.
45. A.K. Maurya, S.M. Pandey, and R. Chhibber, Structure–Property Relationships and Corrosion Behavior of Laser-Welded X-70/UNS S32750 Dissimilar Joint, *Arch. Civ. Mech. Eng.*, 2023, **23**, p 81.
46. X.L. Zhang, J.L. Sun, and J. Luo, Mechanical and Corrosion Behaviour of In Situ Intermetallic Phases Reinforced Mg-Based Glass Composite, *Mater. Sci. Technol.*, 2017, **33**, p 10.
47. M.E. Turan, Y. Sun, and F. Aydin, Effects of Carbonaceous Reinforcements on Microstructure and Corrosion Properties of Magnesium Matrix Composites, *Mater. Chem. Phys.*, 2018, **218**, p 182–188.
48. S.S.M. Mehrian, F. Khodabakhshi, and M. Rahsepar, Electrochemical Corrosion Characteristics of Friction Stir-Reacted Aluminum Matrix Hybrid Nanocomposites, *J. Mater. Res. Technol.*, 2024, **28**, p 1924–1940.
49. M. Rahsepar and Y. Jarahimoghadam, The Influence of Multipass Friction Stir Processing on the Corrosion Behavior and Mechanical Properties of Zircon-Reinforced Al Metal Matrix Composites, *Mater. Sci. Eng. A*, 2016, **671**, p 214–220.
50. A. Rao, V. Katkar, G. Gunasekaran, V. Deshmukh, N. Prabhu, and B. Kashyap, Effect of Multipass Friction Stir Processing on Corrosion Resistance of Hypereutectic Al–30Si Alloy, *Corros. Sci.*, 2014, **83**, p 198–208.

51. M.M. El-Rayes and E.A. El-Danaf, The Influence of Multi-pass Friction Stir Processing on the Microstructural and Mechanical Properties of Aluminum Alloy 6082, *J. Mater. Process. Technol.*, 2012, **212**, p 1157–1168.

Publisher's Note Springer Nature remains neutral with regard to jurisdictional claims in published maps and institutional affiliations.

Springer Nature or its licensor (e.g. a society or other partner) holds exclusive rights to this article under a publishing agreement with the author(s) or other rightsholder(s); author self-archiving of the accepted manuscript version of this article is solely governed by the terms of such publishing agreement and applicable law.